Evaluation of bent-crystal x-ray backlighting and microscopy techniques for the Sandia Z machine

Daniel B. Sinars, Guy R. Bennett, David F. Wenger, Michael E. Cuneo, and John L. Porter

X-ray backlighting and microscopy systems for the 1–10-keV range based on spherically or toroidally bent crystals are discussed. These systems are ideal for use on the Sandia Z machine, a megajoule-class x-ray facility. Near-normal-incidence crystal microscopy systems have been shown to be more efficient than pinhole cameras with the same spatial resolution and magnification [Appl. Opt. **37,** 1784 (1998)]. We show that high-resolution ($\leq$10 μm) x-ray backlighting systems using bent crystals can be more efficient than analogous point-projection imaging systems. Examples of bent-crystal-backlighting results that demonstrate 10-μm resolution over a 20-mm field of view are presented.

OCIS codes: 110.7440, 340.7440, 350.5400.

1. Introduction

Spectroscopic diagnostics for the 1–10-keV range based on bent crystals have been routinely employed since the 1930s.[1,2] Such diagnostics are based on the Bragg diffraction of x rays from crystal planes. Only x rays satisfying the Bragg condition,

$$n\lambda = 2d \sin \theta, \tag{1}$$

are reflected from the surface of the crystal. In Eq. (1), λ is the incident photon wavelength, d is the spacing of planes in the crystal, θ is the grazing angle (the angle with respect to the crystal plane), and n is an integer corresponding to the crystal's reflection order.

More recently, however, imaging schemes that use bent crystals have been employed for self-emission microscopy[3] and backlighting.[4,5] The narrow spectral bandwidth of such imaging configurations, $(\Delta\lambda/\lambda) \sim 10^{-3}$–$10^{-4}$, allows images to be obtained in essentially monochromatic light. Most of the progress in the field of crystal-based imaging diagnostics is relatively recent, occurring only within the past decade.

In a microscopy configuration, an image of the self-emission from a bright x-ray source (usually a plasma) is obtained by use of a bent crystal. A recent example of this is work by Uschmann *et al.*,[6] in which an array of toroidally bent Si and Ge crystals were used to obtain five gated, two-dimensional images of an Ar plasma in Ar Ly_β and Ar He_β line radiation. Coupled with high-resolution x-ray spectroscopy, this microscopy diagnostic allowed Uschmann *et al.* to determine time-dependent density gradients in an imploding Ar-doped, inertial-confinement-fusion (ICF) capsule.[7] Lawrence Livermore National Laboratories is actively investigating bent-crystal microscopy for similar applications on the National Ignition Facility currently under construction.[8]

Bent crystals can also be used as part of a backlighting diagnostic. In this case, a two-dimensional image of a dense plasma object is created with the emission from a separate backlighting source, such as a laser-produced plasma or an x pinch.[4,5] Recently this technique was used to backlight CH planar targets at the Nike laser facility.[9,10] The experiments used a laser-produced plasma as a source of Si He_α x rays (1.865 keV) and obtained 2–3-μm-image spatial resolution over a several-millimeter field of view (FOV).

This paper discusses the application of bent-crystal imaging techniques to the Z machine located at Sandia National Laboratories in Albuquerque, New Mexico. The Z machine is a 20-MA pulsed-power driver

D. Sinars (dbsinar@sandia.gov), D. Wenger, M. Cuneo, and J. Porter are with Sandia National Laboratories, P.O. Box 5800, Albuquerque, New Mexico 87185-1193. G. Bennett is with Ktech Corporation, 2201 Buena Vista SE, Suite 400, Albuquerque, New Mexico 87106-4265.

Received 5 July 2002; revised manuscript received 9 December 2003.

0003-6935/03/194059-13$15.00/0

for imploding wire-array z pinches[11] and is capable of producing x-ray powers up to 230 TW and total x-ray yields up to 1.8 MJ.[12] This is the first time that bent-crystal imaging techniques have been applied for use with a megajoule-class source of x rays, and we show that they are ideally suited for use with such intense x-ray sources. Although bent-crystal x-ray backlighting of wire-array z-pinch implosions was proposed some time ago,[13] it was not pursued until now. Here we present one of the first images of a wire-array implosion on the Sandia Z machine. Future planned applications include backlighting and microscopy of ICF targets.

X-ray backlighting experiments on the Z machine use the Z-Beamlet laser facility located in an adjacent building. The Z-Beamlet laser will ultimately be capable of producing >2 kJ of 2ω energy ($\lambda = 527$ nm) in up to four pulses of <2-ns total duration in a 20-ns interval. Up to 80% of this energy can be focused into a ~50-μm-diameter focal spot, resulting in an irradiance of $>4 \times 10^{16}$ W/cm^2.[14] Although not yet at full capacity, the Z-Beamlet laser has already successfully been used as a source of 4.75- and 6.7-keV x rays for point-projection backlighting of ICF capsule targets driven by the Z machine.[15]

Analytic expressions for evaluating the efficiency of x-ray microscopy techniques that use bent crystals have already been derived.[8] Many, but not all, of these are directly applicable to x-ray backlighting configurations. Several of the expressions for microscopy systems are reproduced here, along with revised expressions relevant to x-ray backlighting. These analytical expressions are used to compare the efficiency of bent-crystal diagnostics with more traditional alternatives—pinhole-camera imaging or point-projection backlighting. Several specific examples that are relevant to current or future experiments at Sandia are considered.

To evaluate the systems considered here, it is necessary to compare systems capable of obtaining the same image parameters (e.g., FOV, magnification, spatial resolution). A diagnostic-independent metric of the efficacy of a given technique is the ratio of the image exposure I to the source brightness B_0, which can be written generally as

$$\frac{I}{B_0} = \frac{\eta\Omega}{M^2}, \tag{2}$$

where Ω is the collection solid angle in steradians; M is the system magnification, and η is the collection efficiency of the optics, including losses due to reflectivity and spectral-bandwidth limitations. Assuming that the optical systems being considered meet the desired FOV requirements, the system with the larger value for the ratio expressed in Eq. (2) is the more efficient system.

Expressions for the parameters in the ratio I/B_0 are presented in Sections 2 and 3 for bent-crystal microscopy and backlighting systems, as well as for their traditional alternatives, pinhole-camera and point-projection imaging. In Section 4, these expressions are used to evaluate several designs for existing or proposed diagnostics on the Z machine. Example experimental results from a bent-crystal backlighting system based on the Si He$_\alpha$ line at 1.865 keV are also presented. Finally, in Section 5, we discuss the implications of these results for future applications of these techniques to Z and Z-Beamlet experiments.

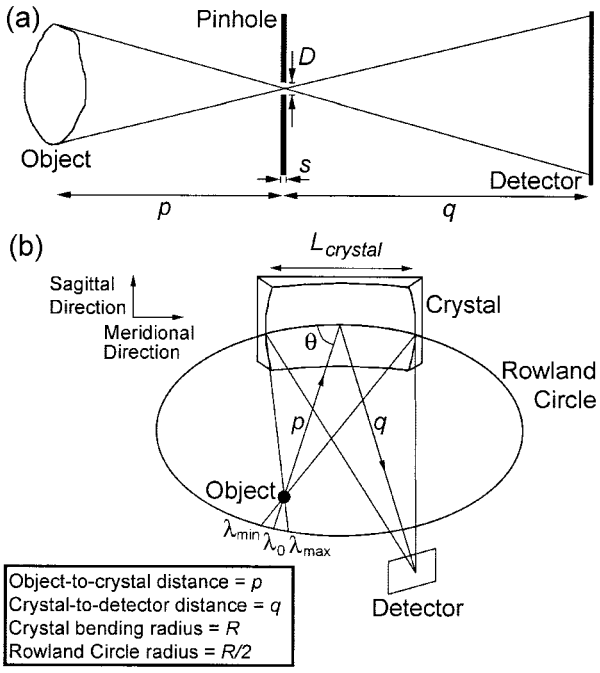

Fig. 1. (a) Schematic diagram depicting a generic pinhole-camera system. (b) Schematic diagram depicting a generic x-ray microscopy system using a spherically or toroidally bent crystal.

2. Geometrical Constraints

A. Self-Emission Imaging Techniques

1. *Pinhole Cameras*

A diagram depicting a generic pinhole-camera system is shown in Fig. 1(a). For a pinhole of diameter D located a distance p from the object, the collection solid angle is

$$\Omega = \frac{(\pi/4)D^2}{p^2}. \tag{3}$$

The spatial resolution obtainable with pinhole cameras can be approximated in the far-field (Fraunhoffer) diffraction limit as

$$\sigma^2 \approx {\sigma_{\text{geom}}}^2 + {\sigma_{\text{diff}}}^2 = \left[\frac{(M+1)D}{M}\right]^2 + \left(\frac{2.44\lambda p}{D}\right)^2, \tag{4}$$

where λ is the wavelength used for imaging. The far-field limit is appropriate for most practical systems on Z, in which the pinhole must be located a relatively large distance from the x-ray source.

Combining Eqs. (3) and (4), it is possible to show[8] that the maximum source distance p for achieving a desired source resolution σ is

$$p_{\max} = \frac{M\sigma^2}{4.88\lambda(M+1)}. \tag{5}$$

The FOV of a pinhole is geometrically limited by the thickness of the substrate and is

$$\mathrm{FOV} = \frac{2pD}{s}, \tag{6}$$

where s is the substrate thickness. In real systems the minimum substrate thickness is often limited by the need to block high-energy x rays.

2. X-Ray Microscopy with Bent Crystals

The general concept of x-ray microscopy with bent crystals is shown in Fig. 1(b). In Fig. 1(b), the object is placed inside the Rowland circle a distance p from the crystal, where p must satisfy

$$R_m \sin\theta > p > \frac{R_m}{2}\sin\theta, \tag{7}$$

R_m is the bending radius of the crystal in the meridional plane, and θ is the Bragg angle. The crystal-to-detector distance is defined as q. The lens equation in the horizontal (meridional) and vertical (sagittal) planes of the crystal are

$$\frac{1}{p} + \frac{1}{q_m} = \frac{2}{R_m \sin\theta}, \tag{8}$$

$$\frac{1}{p} + \frac{1}{q_s} = \frac{2\sin\theta}{R_s}, \tag{9}$$

respectively. If $R_s = R_m \sin^2\theta$ (i.e., a toroidally bent crystal is used), then $q_s = q_m$, and astigmatism is reduced to a minimum. Alternatively, $q_s = q_m$ also occurs if $\theta = 90°$. If θ is in the range from 80° to 90°, however, a spherical crystal ($R_s = R_m$) can be used with a relatively small amount of astigmatism sufficient to obtain micrometer scale spatial resolution.[5] Thus in this range there is little difference in the performance of spherically and toroidally bent crystals. For Bragg angles $<80°$, toroidally bent crystals are preferred.

The magnification in the meridional plane is given by

$$M_m = \frac{q - R\sin\theta}{R\sin\theta - p}, \tag{10}$$

and in the sagittal plane by

$$M_s = \frac{q}{p}. \tag{11}$$

In the case of a toroidally bent crystal, where $q = q_m = q_s$, $M_s = M_m$. For a spherically bent crystal, $M_s = M_m$ only if the detector distance $q = q_m$ in Eq. (8). From Eqs. (8) and (11) one can also derive the following simple relationship:

$$p = \frac{(R\sin\theta)(M+1)}{2M}. \tag{12}$$

By using the light-path formalism presented in Ref. 16, we can estimate the spatial resolution in the sagittal and meridional directions for spherical mirrors. In the vertical direction, the spatial resolution is given by

$$\sigma = \frac{L_s(M+1)(1-\sin^2\theta)}{M}. \tag{13}$$

Because of the choice to use Eq. (8) to determine the position of the detector, there is no astigmatism in the meridional direction, and the spatial resolution is limited by coma and higher-order aberrations. Thus the spatial resolution in the meridional plane is better than that predicted by Eq. (13). The aperture L_s in Eq. (13) is determined by the collection solid angle. In microscopy configurations, Ω is usually limited by the dimensions of the crystal, whereas in backlighting configurations the collection solid angle usually limits L_s to a value less than the crystal's dimensions. We note that the spatial resolution estimated by Eq. (13) should be regarded only as an approximation, the actual spatial resolution can be better. For example, the spatial resolution in the sagittal direction predicted by Eq. (13) for the backlighting system fielded by Aglitskiy *et al.*[9,10] is $\sim$10 μm, but the experimental results measured spatial resolutions of 2–3 μm over the entire FOV.

The FOV of a microscopy system can be estimated[8] to be

$$\mathrm{FOV} = 2p\left(\frac{\Delta\lambda}{\lambda}\right)\tan\theta. \tag{14}$$

B. Backlighting Imaging Techniques

1. Point-Projection Backlighting

A diagram of a generic point-projection backlighting system is shown in Fig. 2(a). This technique is the simplest system for radiography and is very easy to align because there are no optical components. The collection solid angle in this system is given by

$$\Omega = \frac{(\pi/4)(\Delta x)^2}{p^2}, \tag{15}$$

where Δx is the diameter of the x-ray source and p is the distance between the source and the object. The spatial resolution of the image is approximately

$$\sigma = (\Delta x)\frac{M-1}{M}. \tag{16}$$

Both of these equations depend on the size of the x-ray source. As Δx is decreased, the spatial resolution of the image improves, but the collection solid angle also decreases, making the system less effi-

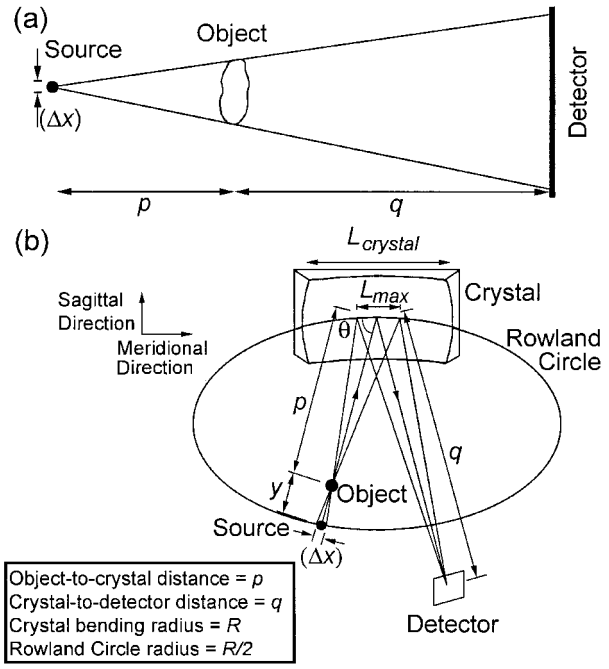

Fig. 2. (a) Schematic diagram depicting a generic point-projection backlighting system. (b) Schematic diagram depicting the meridional plane of a generic x-ray backlighting system using a spherically or toroidally bent crystal.

cient. Unlike the other systems considered here, the FOV of the point-projection backlighting system is limited only by collection apertures or the size of the detector.

2. *Bent-Crystal X-Ray Backlighting*

A generic x-ray backlighting system that uses a spherically bent crystal is shown in Fig. 2(b). The distance between the object and the crystal is p, the distance between the image and the crystal is q, and the distance between the source and the object is y. If the source is located on the Rowland circle,

$$y = R \sin \theta - p. \tag{17}$$

As noted by Aglitskiy *et al.*,[9,10] however, it is not necessary for the backlighting source to lie on the Rowland circle. If the x-ray source is moved inside the Rowland circle, the spectral bandwidth and collection solid angle both increase, making the system more efficient. The penalty is a reduced FOV and worse spatial resolution. This is discussed further in Sections 4 and 5.

The position of the object and the detector in bent-crystal backlighting is determined by Eq. (8) as in bent-crystal microscopy. Similarly, the spatial resolution can be estimated with Eq. (13), except that L is usually determined by the collection solid angle given by

$$\Omega = \frac{(\pi/4)(\Delta x)^2}{y^2}, \tag{18}$$

so that

$$L = \frac{(\Delta x)p}{y}. \tag{19}$$

The FOV of the backlighting system can be estimated as

$$\mathrm{FOV} = L_{\mathrm{crystal}}\left(\frac{y}{p+y}\right), \tag{20}$$

where L_{crystal} is the width of the crystal in the meridional or sagittal direction.

3. Imaging System Efficiency

As expressed in Eq. (2), the geometrical limitations to the collection angle of the system are not the only parameters it is necessary to consider. Reflective surfaces, for example, seldom reflect 100% of the incident radiation. Furthermore, there may be limitations to the spectral bandwidth passed by the optics. These additional reductions to the image exposure I in Eq. (2) are expressed in terms of an efficiency parameter η.

In general, systems without optical components have $\eta = 1$ because there are no reflective surfaces or bandwidth limitations. This is the case for pinhole-camera imaging and is usually also the case for point-projection imaging. However, it is not always possible to generate a backlighter source with very small dimensions. In this case, a pinhole with dimensions smaller than the backlighter source can be employed to create an effective source size small enough to obtain the desired spatial resolution. This effectively reduces the brightness of the backlighter source, which can be expressed as part of the efficiency parameter η. If the pinhole is close to the source,

$$\eta \approx \frac{D^2}{(\Delta x)^2}, \tag{21}$$

where D is the pinhole's diameter and Δx is the size of the source. In real systems, one must always be concerned about surface ablation of the pinhole's substrate by the source radiation, which can effectively reduce or close the pinhole's aperture. Other methods exist to reduce the source size for laser-produced plasmas, such as irradiating a small-diameter fiber. Such a system is somewhat inefficient at converting the laser energy into x rays and may also suffer from reduced spatial resolution if the fiber expands during the pulse.

The microscopy and backlighting systems considered here rely on mirrors based on Bragg diffraction. The efficiency of Bragg optics varies with the perfection of the crystal, commonly expressed in terms of the width of the crystal's rocking curve ($\Delta\lambda_{\mathrm{Bragg}}$). For simplicity, we assume that the reflected radiation is evenly distributed across the width of the rocking curve (i.e., a square-shaped rocking-curve function). We also assume that the spectral-line shape of the

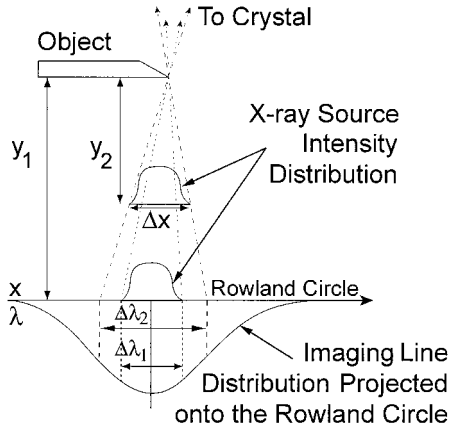

Fig. 3. Schematic illustrating how the size of the x-ray source in a bent-crystal backlighting scheme can limit the spectral bandpass of the system to less than the width of the line used for imaging. If the x-ray source is on the Rowland circle, its width (Δx) determines the spectral bandpass used for imaging ($\Delta\lambda_1$). Moving the source off the Rowland circle can effectively increase the spectral bandpass of the system as shown to $\Delta\lambda_2$.

source is square shaped so that the source energy is evenly distributed across the width of the spectral-line shape ($\Delta\lambda_{\text{line}}$). For near-normal-incidence mirrors, $\Delta\lambda_{\text{line}} \gg \Delta\lambda_{\text{Bragg}}$ usually holds, so

$$\eta = \frac{R_{\text{int}}}{(\Delta\lambda_{\text{line}}/\lambda)\tan\theta}, \tag{22}$$

where R_{int} is the integrated reflectivity of the crystal, $\Delta\lambda_{\text{line}}/\lambda$ is the relative spectral linewidth of the x-ray line used for backlighting, and θ is the Bragg angle. In many imaging systems, Eq. (22) must be multiplied by an additional parameter η_{line} because the spectral bandwidth passed by the optics is less than the spectral bandwidth of the source. This is true if

$$L < L_{\text{line}} = \frac{(\Delta\lambda_{\text{line}}/\lambda)Rp\,\tan\theta}{R\,\sin\theta - p}, \tag{23}$$

in which case

$$\eta_{\text{line}} = \frac{L}{L_{\text{line}}} = \frac{\Delta\lambda/\lambda}{\Delta\lambda_{\text{line}}/\lambda}, \tag{24}$$

$$\eta = \frac{R_{\text{int}}\eta_{\text{line}}}{(\Delta\lambda_{\text{line}}/\lambda)\tan\theta}. \tag{25}$$

This situation is illustrated in Fig. 3 for a generic bent-crystal imaging geometry. Because the spatial size of the x-ray source projected on the Rowland circle is smaller than the width of the spectral line used for imaging (as projected on the Rowland circle), Eq. (25) must be used to take this inefficiency into account. As noted above, it is possible to move the source off the Rowland circle (i.e., decrease the distance y between the source and the object). This can increase the efficiency of the system, as seen in Fig. 3. Examples illustrating this effect are discussed in Section 4. If the source and the object are the same, as in microscopy, then the spectral range used for imaging is determined by the size of the crystal projected through the object to the Rowland circle. In microscopy it is usually possible to use the entire width of the spectral line. Equations (22)–(25) hold for both microscopy and backlighting configurations. For most of the cases considered in Section 4, it is necessary to use Eq. (25) in place of Eq. (22). For bent-crystal backlighting configurations, η_{line} is usually easier to calculate in terms of the spectral bandpass of the system (derived from the Bragg equation),

$$\frac{\Delta\lambda}{\lambda} \approx \frac{\Delta x}{R\,\tan\theta}. \tag{26}$$

With Eq. (26), η can be rewritten as

$$\eta = \left[\frac{R_{\text{int}}}{(\Delta\lambda_{\text{line}}/\lambda)^2\,\tan^2\theta}\right]\left(\frac{\Delta x}{R}\right). \tag{27}$$

4. Discussion

Before this work, all previous applications of bent-crystal imaging techniques had been with sources or objects that produce <1000 J of x rays. In contrast, wire-array z pinches on the Z machine produce 1–2 MJ of x rays in a near-Planckian spectrum that includes an intense x-ray bremsstrahlung background in the 0.01–1-MeV range. Z pinches are also strong sources of debris. Adapting bent-crystal imaging techniques to the Z machine required the consideration of a number of practical constraints. In this section we discuss the design of several imaging diagnostics for the Z machine that have been built or are under consideration for future development.

One design constraint is the pulsed-power geometry. Portions of the pulsed-power hardware lie in the horizontal plane of the load. Most of the primary diagnostics are located along one of nine lines of sight angled up 12° from the horizontal plane, as indicated in Fig. 4(a). It is possible to field diagnostics in the horizontal plane only if they fit inside the 1.25-m-radius vacuum chamber. To mitigate the high-velocity, expanding debris created after the z-pinch implosion, a blast shield ~0.5 m in diameter is usually used. Diagnostic components, such as crystals, that lie within this blast shield are destroyed and must be replaced after each test.

Although it would be ideal to locate crystals outside of the blast shield, this was deemed to be impractical. According to Eq. (7), the object must be located no farther than $R\,\sin\theta$ from the crystal, which would require a bending radius >900 mm to place the crystal outside the blast shield. To obtain a large FOV, a large, perfectly bent crystal would be required. It is not always possible to obtain very large crystal sheets, and as the surface area and bending radius increase it becomes increasingly difficult to bend crystals uniformly across the entire surface area. Another difficulty is that for a fixed spatial resolution the limits on the mosaicity of the crystal become more stringent with increasing working distance, as noted by Koch *et al.*[8] and observed experimentally.[5] Main-

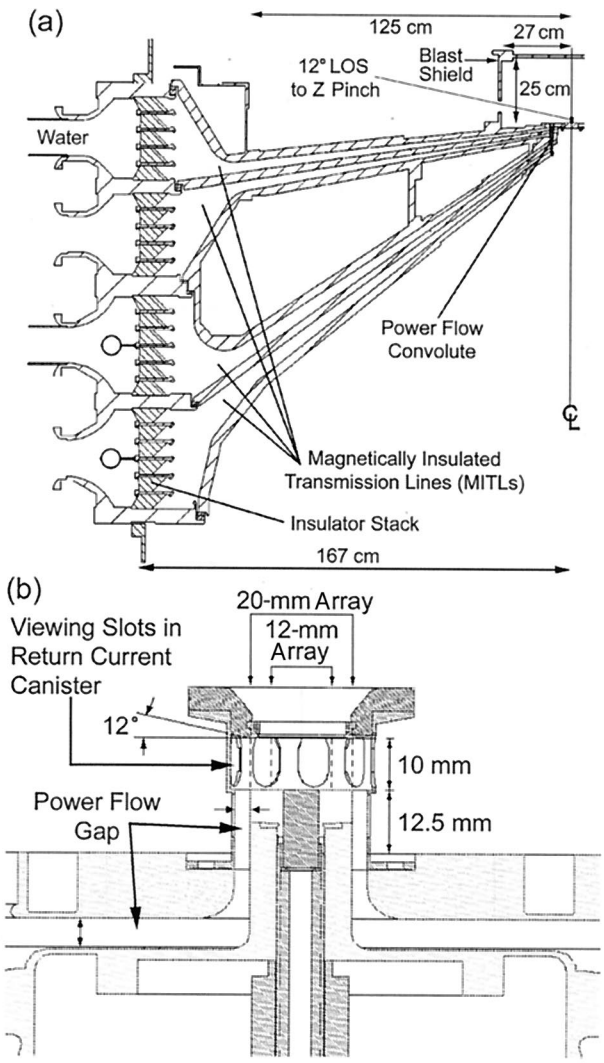

Fig. 4. (a) Cross section of the Z machine, showing the final stages of the pulsed-power feeds that deliver current to the wire-array load. The machine is cylindrically symmetric about the marked centerline. The blast shield used to confine debris is also shown. The pulsed-power hardware restricts the area available for diagnostics in the horizontal plane to a 125-cm radius. As a result, most diagnostics are mounted in one of nine viewing lines of sight (LOS) located at a 12° angle. (b) Expanded cross-section view of the region near the wire array, showing the return-current canister, the power feeds, and the location of 20- and 12-mm-diameter wire arrays. The example shown is a raised load, placing the mid-height of the wire array at the height of the backlighter detector.

taining a high spatial resolution with a crystal with a large bending radius would require a crystal with a very narrow rocking curve. In practice, crystals with bending radii >250 mm and diameters >40 mm are seldom used in experiments, although good results have been obtained with quartz crystals with bending radii up to 500 mm.[17]

Based on the above considerations, several imaging systems that use crystals with bending radii of 250 mm were designed. The detector position of these systems was chosen to be compatible with existing detector hardware that placed the detector (usually film) in a W shutter box outside the blast shield. Several promising crystal–emission-line combinations useful for backlighting and microscopy applications on the Z machine were considered, including several under consideration for the National Ignition Facility, which will also be a megajoule-class x-ray source.[8] Comparable point-projection and pinhole-camera systems with the same magnification and detector distances were also evaluated. The results of these calculations are presented in Tables 1, 2, 3, and 4.

Table 1 presents calculations for several bent-crystal backlighting systems. One of these, the 1.865-keV Si He_α system, has been developed and used during Z experiments. This system is similar to the backlighting diagnostic used by Aglitskiy *et al.*[9,10] at the Naval Research Laboratory. Tests on the Z-Beamlet laser that used the 6.18-keV Mn He_α system described in Table 1 have recently begun. Although the flux reaching the detector is relatively low, this system shows promise as a backlighter for future Z-machine experiments.

To evaluate the efficiency of the systems presented in Table 1 we made reasonable estimates for the parameters of Z-Beamlet-produced x-ray sources. For low-energy x-ray systems, such as the Si He_α system, larger source sizes (0.5–1 mm) are reasonable. For higher-energy x-ray systems, smaller source sizes are necessary to efficiently convert the laser energy into x rays ($\leq$0.2 mm). At present, typical tests on the Z-Beamlet laser produce about 600 J of laser light. With reasonable estimates for the efficiency of the conversion from laser to x-ray energy, a source brightness was calculated for each of the systems in Table 1. The Si He_α system produces enough flux at the detector to use Kodak RAR 2497 film, but most of the other systems require the more sensitive Kodak DEF film or microchannel-plate–CCD cameras. Our initial tests with the Mn He_α system confirm that DEF film is necessary to obtain an image.

Table 1 also includes estimates for the improved efficiency obtained by moving the source off the Rowland circle, as discussed earlier in Section 2.B. This has the effect of increasing the spectral bandpass transmitted by the bent-crystal system but results in a smaller field of view and poorer spatial resolution. The actual system fielded by Aglitskiy *et al.*[9,10] placed the source 44 mm inside the Rowland circle of a crystal with $R = 200$ mm. As shown in Table 1, this resulted in almost an order-of-magnitude increase in I/B_0, but the spatial resolution nearly doubled and the FOV shrank by about 30%. For the systems considered on the Z machine, it is impractical to mount a laser target closer than ~80 mm from the center of the wire array. Thus we consider the effect of moving the source in the Sandia systems 20 mm inside the Rowland circle. The effect is relatively small, doubling I/B_0.

The alternative to using bent-crystal backlighting is point-projection backlighting. To compare the two techniques, systems with the same image param-

Table 1. Comparison of Several X-Ray Backlighting Systems[a] Relevant to Sandia's Z Machine and the Z-Beamlet Laser

	System A	System B	System C	System D
X-ray source parameters				
Backlighter emission line	Si He_α	Si He_α	Mn He_α	Cu K_α
Source wavelength (Å)	6.65	6.65	2.016	1.541
Estimated linewidth ($\Delta\lambda_{line}/\lambda$)	1.5×10^{-3}	1.5×10^{-3}	5.0×10^{-4}	5.0×10^{-3}
Laser energy (J)	400	600	400	400
Estimated conversion efficiency	0.01	0.01	0.003	0.003
Source diameter (mm)	1.0	0.4	0.4	0.4
Source brightness ($J/mm^2/sr$)	0.41	3.8	0.76	0.76
Imaging hardware parameters				
Crystal	Quartz $10\bar{1}1$	Quartz $10\bar{1}1$	Quartz $22\bar{4}3$	Quartz $21\bar{3}1$
Reflection order	1	1	1	2
Bragg angle (°)	83.9	83.9	84.9	88.7
Integrated reflectivity[b] (mrad)	1.0	1.0	0.078	0.079
Spherical-crystal bending radius (mm)	250	200	250	250
Crystal aperture (mm)	48	10	23	48
System magnification	6	20	6	6
Object-to-crystal distance (mm)	145	105	145	145
FOV (mm)	20	4.75	9.6	20
Calculated efficiency parameters				
Source linewidth ($\Delta\lambda/\lambda$)	4.3×10^{-4}	2.1×10^{-4}	1.4×10^{-3}	3.6×10^{-5}
η_{line}	0.28	0.14	0.29	0.007
Collection solid angle (sr)	7.4×10^{-5}	1.4×10^{-5}	1.2×10^{-5}	1.2×10^{-5}
L_{max} (mm)	1.42	0.45	0.57	0.56
η	2.0×10^{-2}	1.0×10^{-2}	4.0×10^{-3}	2.6×10^{-6}
I/B_0 (sr)	4.2×10^{-8}	3.6×10^{-10}	1.3×10^{-9}	8.4×10^{-13}
Intensity at detector ($photons/\mu m^2$)	57	4.6	1.0	5.0×10^{-4}
DEF Exposure[c] ($photons/\mu m^2$) for OD 1	0.5	0.5	0.33	0.4
RAR 2497 Exposure[d] ($photons/\mu m^2$) for OD 1	4.9	4.9	21	43
Approximate spatial resolution (μm)	9.4	2.7	2.6	0.2
Changes for source off Rowland circle				
Distance inside Rowland circle (mm)	20	44	20	20
FOV (mm)	17.6	3.3	8.4	17.6
I/B_0 (sr)	8.0×10^{-8}	2.4×10^{-9}	2.5×10^{-9}	1.6×10^{-12}
Intensity at detector ($photons/\mu m^2$)	110	31	2.0	9.4×10^{-4}
Approximate spatial resolution (μm)	11.6	5.0	3.2	0.2

[a]The Si He_α system will be tested during upcoming experiments, and the Mn He_α system is under consideration for future tests. The Si He_α system used at the Naval Research Laboratory by Aglitskiy[9] is shown as System B for comparison.
[b]Ref. 18.
[c]Ref. 19.
[d]Ref. 20.

eters were considered. The parameters of a point-projection backlighting system with 10-μm spatial resolution, a magnification of 6, and a detector position of 900 mm is shown in Table 2. Z-Beamlet is designed to have a best-focus spot of 50 μm, so to obtain a 10-μm spatial resolution a 12-μm pinhole diameter is required. Although a point-projection system capable of ~40-μm spatial resolution has an efficiency comparable with the bent-crystal systems under consideration, improving the spatial resolution to 10 μm results in a significant decrease in efficiency.

Bent-crystal microscopy systems are nearly identical to backlighting systems. The primary difference is that instead of detecting x rays from an independent source, the system detects emission from the object itself. As a result, the spectral bandwidth used for imaging is typically larger and is limited by the size of the crystal. This makes microscopy systems more efficient than backlighting systems with the same parameters. This is illustrated in Table 3, which evaluates the efficiency of the same systems considered in Table 1 in a microscopy configuration. Comparing the data in Tables 1 and 3, we see that microscopy systems can be up to 2 orders of magnitude more efficient than backlighting systems with the source on the Rowland circle.

The traditional alternative to bent-crystal microscopy is pinhole-camera imaging. In Table 4, several pinhole-camera systems with parameters analogous to those in Table 3 are presented. It is clear that bent-crystal microscopy systems can be considerably more efficient than pinhole-camera systems, as previously noted by Koch *et al.*[8] For this reason, there is considerable interest in bent-crystal systems for x-ray microscopy.

The estimates for the spatial resolution presented in Table 1 were based on Eq. (13). This analytic expression estimates the aberrations resulting from the use of spherical-mirror optics. These estimates

Table 2. Calculated Results for Point-Projection Backlighting Systems with Parameters Comparable to the Bent-Crystal Backlighting Systems Presented in Table 1

	System A	System B
Standard method		
Source size[a] (μm)	50	50
Source-to-object distance (mm)	100	150
Object-to-detector distance (mm)	500	900
System magnification	6	6
Collection solid angle (sr)	2.0×10^{-7}	8.7×10^{-8}
I/B_0 (sr)	5.5×10^{-9}	2.4×10^{-9}
Approximate spatial resolution (μm)	41.7	41.7
Changes if pinhole used		
Pinhole diameter (μm)	12	12
η	0.058	0.058
Collection solid angle (sr)	1.1×10^{-8}	5.0×10^{-9}
I/B_0 (sr)	1.8×10^{-11}	8.0×10^{-12}
Approximate spatial resolution (μm)	10	10

[a]The 50-μm source size is the minimum focal-spot size obtainable with Z-Beamlet. To obtain 10-μm resolution a 12-μm pinhole can be used in front of the source, at a cost of reduced efficiency.

were checked by carrying out ray-tracing simulations with the ZEMAX program,[22] as well as by obtaining test images of wire meshes in experiments. The results of the ray-tracing simulations are presented in Table 5. The simulations yielded very different resolutions along the vertical (sagittal) and horizontal (meridional) directions. This difference arises as a result of the different focal distances along the two directions. Since the detector was placed at the position of the horizontal focus, the resolution in this direction is very good. The simulations also demonstrated that the spatial resolution worsened for the portions of the image that used the extreme corner of the crystal. This demonstrates the breakdown of the Rowland-circle approximation far from the center of the crystal. The Rowland-circle approximation also begins to break down as the source size increases (thereby increasing the surface area of the crystal contributing to each point in the image), which explains why the resolution worsens with increasing source size.

Experimental tests of the 1.865-keV Si He_α system with a 33.5-μm square-wire Ni mesh were carried out on the Z-Beamlet facility. A portion of a sample image from such a test, along with a lineout across one

Table 3. Comparison of Selected X-Ray Microscopy Systems Relevant to Sandia's Z Machine[a]

	Setup A	Setup B	Setup C	Setup D	Setup E
X-ray source parameters					
Source emission line	Si He_α	Mn He_α	Cu K_α	Ar Ly_β	Ar He_β
Source wavelength (Å)	6.65	2.016	1.541	3.151	3.366
Estimated linewidth ($\Delta\lambda_{line}/\lambda$)	1.5×10^{-3}	5.0×10^{-4}	5.0×10^{-3}	5.0×10^{-4}	5.0×10^{-4}
Imaging hardware parameters					
Crystal	Quartz $10\bar{1}1$	Quartz $22\bar{4}3$	Quartz $21\bar{3}1$	Si 311	Ge 311
Reflection order	1	1	2	1	1
Bragg angle (°)	83.9	84.9	88.7	74.2	80.6
Integrated reflectivity (mrad)	1.0	0.078	0.079	0.100	0.350
Crystal bending radius (mm)	250	250	250	250	250
Crystal aperture (mm)	4.3	4.3	4.3	4.4	4.3
System magnification	6	6	6	6	6
Object-to-crystal distance (mm)	145	145	145	145	145
Approximate FOV (mm)	3.5	3.5	3.6	3.3	3.5
Calculated efficiency parameters					
Source linewidth ($\Delta\lambda/\lambda$)	1.3×10^{-3}	1.1×10^{-3}	2.8×10^{-4}	3.2×10^{-3}	2.0×10^{-3}
η_{line}	0.87	1.00	0.056	1.00	1.00
Collection solid angle (sr)	8.6×10^{-4}	8.6×10^{-4}	8.6×10^{-4}	8.6×10^{-4}	8.6×10^{-4}
η	6.2×10^{-2}	1.4×10^{-2}	2.0×10^{-5}	5.7×10^{-2}	1.2×10^{-1}
I/B_0 (sr)	1.5×10^{-6}	3.3×10^{-7}	4.8×10^{-10}	1.4×10^{-6}	2.8×10^{-6}
Approximate spatial resolution (μm)	10	10	10	10	10

[a]The data for the integrated reflectivity in setups A–C came from Ref. 18 and the reflectivity for setups D–E came from Ref. 21.

Table 4. Calculated Results for Pinhole-Camera Systems at Four Selected Wavelengths[a]

Imaging wavelength (Å)	6.65	2.106	1.541	2.221
Spatial resolution (μm)	23.8	13.3	12.6	13.6
Collection solid angle (sr)	4.8×10^{-9}	4.8×10^{-9}	4.8×10^{-9}	4.8×10^{-9}
I/B_0 (sr)	1.3×10^{-10}	1.3×10^{-10}	1.3×10^{-10}	1.3×10^{-10}

[a]All systems shown have object-to-pinhole distances of 128 mm, a 10-μm-diameter pinhole, and a system magnification of 6. These choices are analogous to the microscopy systems presented in Table 3. The object-to-pinhole distance was chosen to place the detector ~900 mm from the object. The spatial resolution was limited in each case by pinhole diffraction effects.

Table 5. Summary of Numerical Ray-Tracing Simulations of the Si He_α Backlighter from Table 1[a]

Source size	Vertical resolution center (M = 5.78)	Horizontal resolution center (M = 5.98)	Vertical resolution center (M = 5.68)	Horizontal resolution center (M = 5.84)
10-μm test mesh				
Point	0.1	0.2	0.5	0.6
100 μm	1.2	0.2	2.8	1.6
500 μm	4.0	0.2	>5	>5
1 mm	4.5	0.2	>5	>5
33.5-μm test mesh				
800 μm	4.1	0.2	10.4	5.9

[a]The simulations used the ZEMAX ray-tracing program and treated the crystal as a spherical mirror. The values in the table are in μm and represent the width of the slope from 87.5% of peak intensity to 12.5% peak intensity. Results are given for reflections from the center and from the upper left-hand corner of a 48 mm by 11 mm crystal. Simulation results using 10- and 33.5-μm-wide test meshes are shown. The magnification in each direction is given in parentheses.

of the mesh bars demonstrating the spatial resolution, is shown in Fig. 5. The mesh tests demonstrated that spatial resolutions of ~10 μm were possible across the entire 20-mm-by-4.3-mm FOV along both the horizontal and vertical directions. There was a slight difference in the resolution in the extreme corners of the image relative to the center (11–12 μm versus 9 μm), but this difference was not as much as predicted in Table 5. These resolutions are larger than predicted by ray tracing but are similar to the analytic estimates presented in Table 1. The crystal's rocking curve, as well as the probable error in the relative distances between optical components during these tests, likely accounts for the difference between the experiments and simulations.

One of the intended goals of this diagnostic is to measure the dynamics of 20-mm-diameter wire arrays at or near their original locations. If the focus of the optical system is placed at $r = 0$, portions of the wire array then lie as much as 10 mm out of focus. To estimate the effect of measuring such a thick object, ray-tracing simulations were performed for mesh objects moved 5 mm toward or away from the crystal. After the different magnifications were accounted for, the spatial resolution estimated by ray tracing was still ~3–4 μm along both directions. The spatial resolution of experimental tests in which the Ni mesh was moved 5 mm out of focus was ~10 μm, essentially the same as that measured during in-focus tests, indicating that the depth of field of this diagnostic is very large.

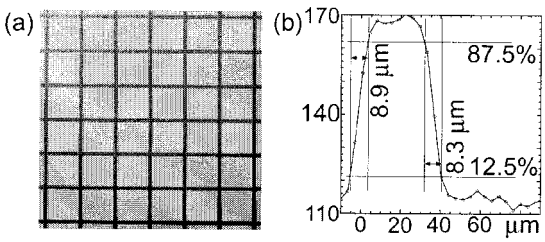

Fig. 5. (a) Backlit image of a 33.5-μm-wide Ni mesh captured on Kodak RAR 2497 film. The 1.865-keV crystal backlighter listed in Table 1 was used with an x-ray source size of 800 μm. (b) Film-density lineout across a single piece of the mesh indicates a spatial resolution of about 10 μm. This spatial resolution was obtained across the entire 20 mm by 4.3 mm FOV of the backlighter.

The 1.865-keV Si He_α backlighting system was successfully used during several recent experiments on the Z machine. The goal of these experiments was to measure the behavior of the wire plasma in cylindrical wire arrays during the earliest stages of the implosions. The dynamics of the earliest wire initiation stages are currently poorly understood, and this diagnostic is proving to be critical to improving our understanding of these initial phases. We briefly consider the practical design of this backlighting diagnostic and explain some of the advantages of this technique for Z-machine applications.

A sample cross-section view of the experimental hardware surrounding the wire array is shown in Fig. 4(b). The current supplied to the Z-machine load flows up through the wire array(s) and returns down the inside surface of a metal canister surrounding the array(s). For diagnostic access, nine viewing slots are typically cut into the canister, coincident with the nine 12° diagnostic lines of sight. The diameter of the return-current canister and the width of the nine slots are selected to obtain a FOV of the wire array(s) that includes an outer edge of both the 20- and 12-mm-diameter arrays. A top-down view of the design showing the position of the 20- and 12-mm-diameter arrays, the return-current canister, and the unblocked x-ray paths through the slots in the return-current canister is presented in Fig. 6. In actual experiments, the FOV through the center pair of slots was reduced on one side by 2 mm by using a 75-μm Au foil over part of the exit aperture. This was done to eliminate any direct line of sight of the center of the array, where the imploding plasma collects and radiates, so as to prevent the crystal from being damaged prematurely due to the intense x-ray flux even during the early stages of the implosion.

A three-dimensional view of the backlighting hardware located inside the blast shield is shown in Fig. 7. The optical components are all mounted on a single ring that is affixed to the anode plate of the Z machine with alignment pins. This design al-

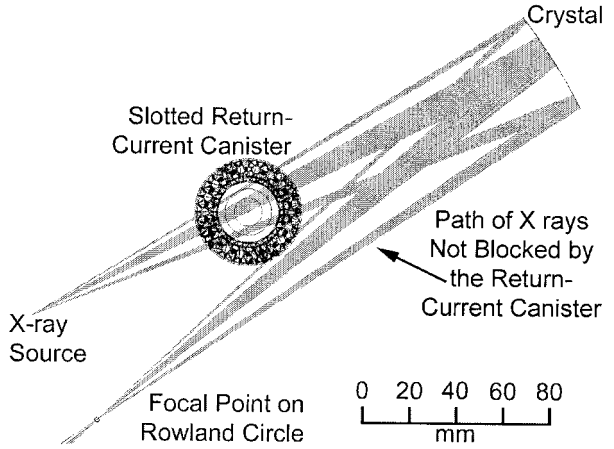

Fig. 6. By use of the ZEMAX ray-tracing program,[22] the FOV for the Si He_α system was estimated. The circles inside the canister indicate the positions of 20- and 12-mm-diameter arrays. Note that if the return-current canister was not present, almost the entire 20-mm wire array could be viewed simultaneously.

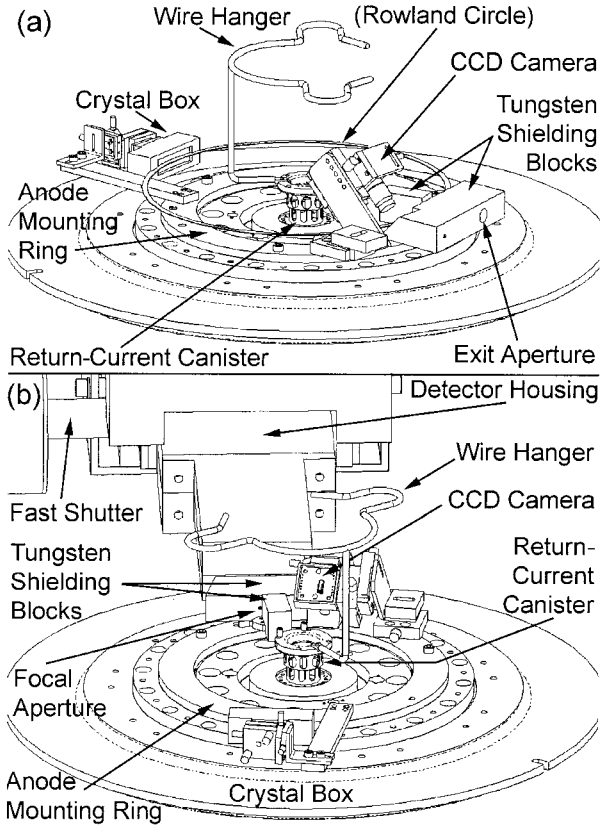

Fig. 7. (a) Three-dimensional view of the hardware for the Si He_α backlighting system. A CCD camera is used to align the focal spot of the laser beam to a target foil (not shown) mounted on the sloped face of the W shielding block. For reference, the 250-mm-diameter Rowland circle is shown superimposed on the hardware. (b) Second view of the hardware, showing the detector system. The crystal focuses the source x rays through an aperture in one of two W shielding blocks. The second block is used to eliminate the direct line of sight between the return-current canister and the aperture. A fast-closing shutter is mounted in the detector housing to prevent particulate debris from reaching the film.

lows the optical system to be aligned and tested outside the Z machine at the Z-Beamlet facility. The Z-Beamlet laser is focused onto a piece of Si mounted on the sloped face of the W shielding. To align the focal spot of the laser, a CCD camera is mounted above the target. The crystal is located in a box on an adjustable mounting. The x rays from the source are focused to the corresponding point on the Rowland circle (shown in Fig. 7 for reference). To prevent high-energy x rays and particulate debris from reaching the detector, thick W shielding blocks are used. A W block is used with a 2- to 4-mm-diameter aperture located at the focal spot on the Rowland circle. A second W block eliminates all direct lines of sight between the return-current canister and this limiting aperture. To further mitigate debris, a fast-closing shutter[23] is mounted in the detector housing. All of the components shown in Fig. 7 are damaged after each experimental test and require replacement or refurbishment.

A sample image from a Z-machine test with the 1.865-keV backlighting diagnostic is shown in Fig. 8. Three portions of the film contain image data from the 300-wire, 20-mm-diameter wire array. These three areas correspond to the three fields of view through the array shown in Fig. 6. This image was taken at approximately 33% of the total implosion time of the array. The wires in the array, which were originally 7.4 μm in diameter, have been vaporized into plasma by the current. Most of the array's mass remains in dense cores ~75 μm in diameter, which are surrounded by tenuous coronal plasma. Azimuthally correlated axial instabilities can be seen developing at the edge of the wire array with a periodic 70-μm structure. Although it is beyond the scope of this manuscript to describe the physics that we can measure with images like this one, we note that these images will be extremely useful for improving the theory and modeling of wire-array z pinches.

5. Conclusions

The data presented in Tables 1 and 2 demonstrate that bent-crystal x-ray backlighting systems can be more efficient than point-projection systems capable of the same spatial resolution and magnification. Although point-projection diagnostics normally have perfect efficiencies, they rapidly become inefficient because the small source size needed to obtain high spatial resolution requires the use of pinholes or other methods. In contrast, although Bragg diffraction from crystal planes is relatively inefficient, bent-crystal imaging systems have relatively large collection angles that compensate for the mirror's inefficiency while maintaining a high spatial resolution.

We note that for bright, laser-produced plasmas of a reasonable diameter, the bent-crystal configurations discussed here do not use the entire width of the

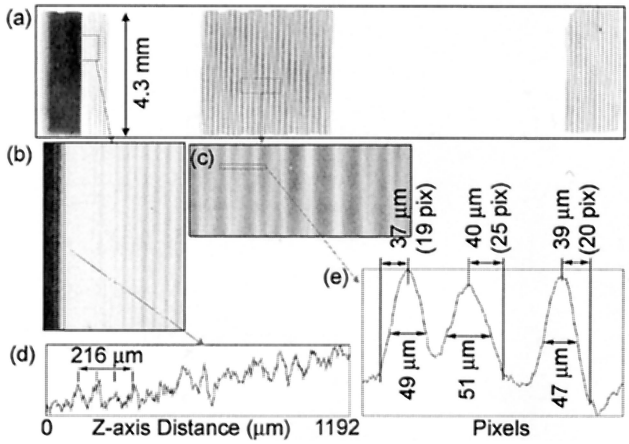

Fig. 8. (a) Backlit image of a 20-mm-diameter, 10-mm-tall, 300-wire array on the Sandia Z machine. The dark regions correspond to x-ray transmission. The image was taken at 83% of the total implosion time of the array, when ~5 MA of current was passing through the array. The wires in the array are still at a radius of 10 mm at this time. (b) Expanded view of the tangential edge of the wire array. (c) Expanded view of the central FOV of the array. Since the focal position of the crystal backlighter is a plane passing through $r = 0$, the wires in this FOV are approximately ±10 mm out of focus and thus have different magnifications. The top of the wire array is rotated 1.6° clockwise with respect to the bottom, creating the angle between the near and far wires. (d) Vertical film-density lineout over the visible axial structure at the edge of the wire array, revealing an azimuthally correlated instability with a period of ~70 μm. (e) Horizontal film-density lineout across selected wires indicates that the wires have expanded from their initial 7.4-μm diameter.

spectral line used for imaging. Thus Eq. (25) holds, and the efficiency of such systems can be written as

$$\frac{I}{B_0} = \left[\frac{R_{\text{int}}}{(\Delta\lambda_{\text{line}}/\lambda)^2 \tan^2\theta}\right]\left[\frac{(\pi/4)(\Delta x)^3}{(p+y)y^2M^2}\right]. \quad (28)$$

In Eq. (28), the parameters in the first bracket are fixed when a particular crystal and emission-line combination are selected. The remaining parameters in the second bracket can be varied to suit the needs of the experimenter. Upon examination of the terms in the second bracket, the most effective way to increase the efficiency of a given system is to move the source closer to the object, as was done in experiments by Aglitskiy *et al.*[9,10] Although it would appear that increasing the source size (Δx) would also increase the efficiency just as quickly, the brightness of most real sources will decrease as $(\Delta x)^2$. It is also clear from Eq. (28) that short working distances are desirable, as noted earlier.

Although the narrow spectral bandwidth of bent-crystal imaging techniques is a disadvantage in that it can make them somewhat inefficient, this is actually an advantage when they are considered for use in today's high-energy x-ray facilities. The Z-Beamlet laser, one of the world's most energetic lasers, only produces a ~0.1–1-J x-ray backlighting source. In contrast, the object being imaged, a wire-array z pinch, produces 1–2 MJ of x rays. To obtain a reasonable signal-to-noise ratio, it is necessary to limit the radiation reaching the detector to the bandwidth emitted by the x-ray backlighter source. Point-projection or pinhole-camera systems can only use plastic or metal filters to restrict the bandwidth of the radiation reaching the detector, but, even when K-edge filters are used, the bandwidth is many times that allowed by bent-crystal systems. Also, such filters do not prevent high-energy x rays in the kilowatt-to-megavolt range (primarily bremsstrahlung radiation) from reaching the detector. Thus bent-crystal imaging systems offer a natural solution to the problem faced by existing and planned megajoule x-ray facilities (such as the National Ignition Facility).

Bent-crystal backlighting systems also offer an advantage in that large FOVs are possible without necessarily increasing the exposure of the detector to debris from the object. The image obtained during the z-pinch experiments, for example, had a 20 mm by 4.3 mm FOV of the object, but a 2–4 mm aperture was used at the focal point on the Rowland circle to limit the detector's exposure to debris. Furthermore, the detector hardware can be collimated to include only the crystal and not the object, again reducing the likelihood of debris's reaching the detector. In contrast, a point-projection system with the same FOV would have to have a detector aperture with a size greater than or equal to the object's size, and the detector would have to be pointed directly at the object.

Currently, only the 1.865-keV bent-crystal backlighting system has been fielded on the Z machine. The initial tests with a 6.18-keV bent-crystal backlighting system have been successful, and we hope to field this higher-energy version on the Z machine by late 2003. Such a system is suitable for looking at the final stages of wire-array z-pinch implosions, and it is also suitable for imaging imploding thin-shell ICF capsules to measure the radiation symmetry of *Hohlraums* on the Z machine. Attempts to measure the latter by using point-projection diagnostics have been hampered by the high-energy bremsstrahlung background.

A practical near-term use for bent-crystal microscopy on the Z machine is imaging selected Ar emission lines from Ar-doped ICF capsule targets, as was done at the GEKKO XII laser facility.[6,21] The Z machine is capable of driving capsule implosions in several different geometries.[15,24,25] Experiments are already under way on the Z machine with Ar-doped capsule targets.[26] Bent-crystal microscopy offers a possible diagnostic technique for imaging Ar emission lines on the Z machine, allowing an analysis similar to that done by Golovkin *et al.*[7] to be performed. Possible parameters for such an imaging system on the Z machine were included in Table 3.

Extending bent-crystal backlighting techniques significantly above 6.18 keV appears to be very challenging. As the wavelength of the backlighter source decreases, it becomes progressively more dif-

ficult to find suitable crystal matches. Most natural crystals have $2d$ spacings greater than 2 Å, necessitating the use of higher-order reflections from crystal planes for energies >6.18 keV. Although higher-order reflections can be used, the reflectivity (R_{int}) decreases with increasing reflection order for most crystals (mica 002 is an exception, see Ref. 27). In addition, the efficiency of the conversion from laser light to x rays rapidly worsens with increasing x-ray energies. Although some alternative sources, such as gas-filled laser targets[28] or x-pinch plasmas,[5] may be more efficient, it is not clear that x-ray backlighting systems with energies >10 keV are feasible.

Until the Z-Beamlet laser is upgraded to a kilojoule-class petawatt laser that is capable of producing efficient K_α x-ray sources, we do not plan to pursue any backlighting systems with energies above 6.18 keV. With a petawatt capability, however, it may be feasible (but difficult) to develop a low-magnification, 8-keV backlighter based on the Cu K_α line. Tests with this crystal–emission-line combination in a microscopy configuration suggest that the reflectivity may be significantly higher than the estimate listed in Table 1.[18] Although it remains to be seen whether higher-energy bent-crystal backlighting systems can be made to work in this near-normal-incidence geometry, it should be possible to use higher-energy bent-crystal microscopy systems because of their inherently greater efficiency.

The authors are grateful to Jeffrey Koch of the Lawrence Livermore National Laboratory for helpful discussions regarding bent-crystal x-ray microscopy. They are also grateful to Sergei Pikuz of the P.N. Lebedev Institute for helpful discussions regarding bent-crystal x-ray backlighting. The authors thank Larry Ruggles and Walt Simpson of Sandia National Laboratories for helpful suggestions regarding the design of the backlighter hardware and for their assistance with the Z-Beamlet calibration tests. Finally, the authors thank the Z-machine operations crew for superb technical support.

References

1. H. H. Johann, "Die Erzeugung lichtstarker Roentgenspektren mit Hilfe von Konkavkristallen," Z. Phys. **69,** 185–206 (1931).
2. V. L. Hamos, "Roentgenspektroskopie und Abbildung mittels gekruemmter Kristallreflektoren," Naturwissenschaften **20,** 705–706 (1932).
3. E. Foerster, K. Gaebel, and I. Uschmann, "X-ray microscopy of laser-produced plasmas with the use of bent crystals," Laser Part. Beams **9,** 135–148 (1991).
4. S. A. Pikuz, T. A. Shelkovenko, V. M. Romanova, D. A. Hammer, A. Y. Faenov, V. A. Dyakin, and T. A. Pikuz, "Monochromatic x-ray probing of an ultradense plasma," JETP Lett. **61,** 638–644 (1995).
5. S. A. Pikuz, T. A. Shelkovenko, V. M. Romanova, D. A. Hammer, A. Y. Faenov, V. A. Dyakin, and T. A. Pikuz, "High-luminosity monochromatic x-ray backlighting using an incoherent plasma source to study extremely dense plasmas," Rev. Sci. Instrum. **68,** 740–744 (1997).
6. I. Uschmann, K. Fujita, I. Niki, R. Butzbach, H. Nishimura, J. Funakura, M. Nakai, E. Foerster, and K. Mima, "Time-resolved ten-channel monochromatic imaging of inertial confinement fusion plasmas," Appl. Opt. **39,** 5865–5871 (2000).
7. I. Golovkin, R. Mancini, S. Louis, Y. Ochi, K. Fujita, H. Nishimura, H. Shirga, N. Miyanaga, H. Azechi, R. Butzbach, I. Uschmann, E. Foerster, J. Delettrez, J. Koch, R. W. Lee, and L. Klein, "Spectroscopic determination of dynamic plasma gradients in implosion cores," Phys. Rev. Lett. **88,** 045002-1–045002-4 (2002).
8. J. A. Koch, O. L. Landen, T. W. Barbee, P. Celliers, L. B. DaSilva, S. G. Glendinning, B. A. Hammel, D. H. Kalantar, C. Brown, J. Seely, G. R. Bennett, and W. Hsing, "High-energy x-ray microscopy techniques for laser-fusion plasma research at the National Ignition Facility," Appl. Opt. **37,** 1784–1795 (1998).
9. Y. Aglitskiy, T. Lehecka, S. Obenschain, S. Bodner, C. Pawley, K. Gerber, J. Sethian, C. M. Brown, J. Seely, U. Feldman, and G. Holland, "High-resolution monochromatic x-ray imaging system based on spherically bent crystals," Appl. Opt. **37,** 5253–5261 (1998).
10. Y. Aglitskiy, T. Lehecka, S. Obenschain, C. Pawley, C. M. Brown, and J. Seely, "X-ray crystal imagers for inertial confinement fusion experiments," Rev. Sci. Instrum. **70,** 530–535 (1999).
11. R. B. Spielman, S. F. Breeze, C. Deeney, M. R. Douglas, F. Long, T. H. Martin, M. K. Matzen, D. H. McDaniel, J. S. McGurn, T. J. Nash, J. L. Porter, L. E. Ruggles, T. W. L. Sanford, J. F. Seamen, W. A. Stygar, J. A. Torres, D. M. Zagar, D. O. Jobe, D. L. Peterson, R. W. Shoup, K. W. Struve, M. Mostrom, P. Cocoran, and I. Smith, "PBFA-Z: a 20-MA z-pinch driver for plasma radiation sources," in *Proceedings of the 11th International Conference on High-Power Particle Beams, Prague, Czech Republic 1996*, K. Jungwirth and J. Ullschmied, eds. (Czech Academy of Sciences, Prague, 1996) Vol. **1,** pp. 150–153 (1996).
12. R. B. Spielman, C. Deeney, G. A. Chandler, M. R. Douglas, D. L. Fehl, M. K. Matzen, D. H. McDaniel, T. J. Nash, J. L. Porter, T. W. L. Sanford, J. F. Seamen, W. A. Stygar, K. W. Struve, S. P. Breeze, J. S. McGurn, J. A. Torres, D. M. Zagar, T. L. Gilliland, D. O. Jobe, J. L. McKenney, R. C. Mock, M. Vargas, T. Wagoner, and D. L. Peterson, "Tungsten wire-array z-pinch experiments at 200 TW and 2 MJ," Phys. Plasmas **5,** 2105–2111 (1998).
13. S. A. Pikuz, T. A. Shelkovenko, D. A. Hammer, and D. F. Acton, "Monochromatic x-ray backlighting for application to PBFA-Z," AIP Conf. Proc. **409,** 523–526 (1997).
14. G. R. Bennett, O. L. Landen, R. F. Adams, J. L. Porter, L. E. Ruggles, W. W. Simpson, and C. Wakefield, "X-ray imaging techniques on Z using the Z-Beamlet laser," Rev. Sci. Instrum. **72,** 657–662 (2001).
15. G. R. Bennett, M. E. Cuneo, R. A. Vesey, J. L. Porter, R. G. Adams, R. A. Aragorn, J. H. Hammer, D. L. Hanson, M. J. Hurst, P. Rambo, D. C. Rovang, L. E. Ruggles, I. C. Smith, W. W. Simpson, D. B. Sinars, S. C. Speas, and D. F. Wenger, "Symmetric inertial confinement fusion capsule implosions in a double-z-pinch-driven Hohlraum," Phys. Rev. Lett. **89,** 245002-1–245002-4 (2002).
16. T. Harada and T. Kita, "Mechanically ruled aberration-corrected concave gratings," Appl. Opt. **19,** 3987–3993 (1980).
17. A. Faenov, VNIIFTRI Institute, Moscow Region, 141570, Russia, and S. Pikuz, P. N. Lebedev Physical Institute, Moscow 117924, Russia (personal communication, 2002).
18. J. A. Koch, Lawrence Livermore National Laboratory, Livermore, Calif. 94551 (personal communication).
19. B. L. Henke, J. Y. Uejio, G. F. Stone, C. H. Dittmore, and F. G. Fujiwara, "High-energy x-ray response of photographic films: models and measurement," J. Opt. Soc. Am. B **3,** 1540–1550 (1986).
20. B. L. Henke, F. G. Fujiwara, M. A. Tester, C. H. Dittmore, and

M. A. Palmer, "Low-energy x-ray response of photographic films. II. Experimental characterization," J. Opt. Soc. Am. B **1,** 828–849 (1984).
21. I. Uschmann, E. Foerster, H. Nishimura, K. Fujita, Y. Kato, and S. Nakai, "Temperature mapping of compressed fusion pellets obtained by monochromatic imaging," Rev. Sci. Instrum. **66,** 734–736 (1995).
22. ZEMAX Optical Design Program, Focus Software Inc., P.O. Box 18228, Tucson, AZ, 85731.
23. D. C. Rovang, W. W. Simpson, L. E. Ruggles, and J. L. Porter, "An electromagnetic fast shutter system for debris mitigation on Z," in *Digest of Technical Papers, 13th IEEE International Pulsed Power Conference, 17–22 June 2001, Las Vegas, Nev.* (Institute of Electrical and Electronics Engineers Nuclear and Plasma Sciences Society, New York, 2001), p. 274.
24. M. K. Matzen, C. Deeney, R. J. Leeper, J. L. Porter, R. B. Spielman, G. A. Chandler, M. S. Derzon, M. R. Douglas, D. L. Fehl, D. E. Hebron, T. J. Nash, R. E. Olson, L. E. Ruggles, T. W. L. Sanford, J. F. Seamen, K. W. Struve, W. A. Stygar, and D. L. Peterson, "Fast z-pinches as dense plasma, intense x-ray sources for plasma physics and fusion applications," Plasma Phys. Controlled Fusion **41,** A175–A184 (1999).
25. M. E. Cuneo, R. A. Vesey, J. L. Porter, G. R. Bennett, D. L. Hanson, L. E. Ruggles, W. W. Simpson, G. C. Idzorek, W. A. Stygar, J. H. Hammer, J. J. Seamen, J. A. Torres, J. S. McGurn, and R. M. Green, "Double z-pinch Hohlraum drive with excellent temperature balance for symmetric inertial confinement fusion capsule implosions," Phys. Rev. Lett. **88,** 215004-1–215004-4 (2002).
26. J. E. Bailey, Sandia National Laboratories, Albuquerque, N.Mex. 87185 (personal communication).
27. G. Hoelzer, O. Wehrhan, J. Heinisch, E. Foerster, T. A. Pikuz, A. Y. Faenov, S. A. Pikuz, V. M. Romanova, and T. A. Shelkovenko, "Flat and spherically bent muscovite (mica) crystals for x-ray spectroscopy," Phys. Scr. **57,** 301–309 (1998).
28. C. A. Back, J. Grun, C. Decker, L. J. Suter, J. Davis, O. L. Landen, R. Wallace, W. W. Hsing, J. M. Laming, U. Feldman, M. C. Miller, and C. Wuest, "Efficient multi-keV underdense laser-produced plasma radiators," Phys. Rev. Lett. **87,** 275003-1–275003-4 (2001).